SSR Damping Controller Design and Optimal Placement in Rotor-Side and Grid-Side Converters of Series-Compensated DFIG-Based Wind Farm

Hossein Ali Mohammadpour, *Student Member, IEEE*, and Enrico Santi, *Senior Member, IEEE*

***Abstract*—This paper deals with subsynchronous resonance (SSR) phenomena in a capacitive series-compensated DFIG-based wind farm. Using both modal analysis and time-domain simulation, it is shown that the DFIG wind farm is potentially unstable due to the SSR mode. In order to damp the SSR, the rotor-side converter (RSC) and grid-side converter (GSC) controllers of the DFIG are utilized. The objective is to design a simple proportional SSR damping controller (SSRDC) by properly choosing an optimum input control signal (ICS) to the SSRDC block, so that the SSR mode becomes stable without decreasing or destabilizing the other system modes. Moreover, an optimum point within the RSC and GSC controllers to insert the SSRDC is identified. Three different signals are tested as potential ICSs including rotor speed, line real power, and voltage across the series capacitor, and an optimum ICS is identified using residue-based analysis and root-locus method. Moreover, two methods are discussed in order to estimate the optimum ICS, without measuring it directly. The studied power system is a 100 MW DFIG-based wind farm connected to a series-compensated line whose parameters are taken from the IEEE first benchmark model (FBM) for computer simulation of the SSR. MATLAB/Simulink is used as a tool for modeling and designing the SSRDC, and power system computer aided design/electromagnetic transients including dc (PSCAD/EMTDC) is used to perform time-domain simulation for design process validation.**

***Index Terms*—Doubly fed induction generator (DFIG), eigenvalue analysis, subsynchronous resonance (SSR), sustainable energy, wind power.**

I. Introduction

DUE to the recent rapid penetration of wind power into the power systems, some countries in central Europe, e.g., Germany, have ran out of suitable sites for onshore wind power projects, due to the high population density in these countries [1]–[4]. Moreover, it has been found that the offshore wind power resources are much larger than onshore wind power sources [2], [4]. Therefore, offshore wind farms have a great potential as large-scale sustainable electric energy resources [5]. One promising solution for offshore wind farm is that of doubly fed induction generator (DFIG), which has gained recent attention of the electric power industry [6]–[9].

Because of their larger size and breadth, offshore wind farms require higher voltage and more robust transmission schemes to achieve adequate efficiency [4], [10]. The transmission system options to transmit the wind power to the shore are high-voltage ac (HVAC) or high-voltage dc (HVDC) [11]–[15]. Studies show that transmitting the offshore wind power through less-expensive HVAC is technically feasible for distances larger than 250 km, if series-capacitive compensation is provided for the transmission line [4].

However, a factor hindering the extensive use of series-capacitive compensation is the potential risk of subsynchronous resonance (SSR) [16]–[22]. The SSR is a condition where the wind farm exchanges energy with the electric network, to which it is connected, at one or more natural frequencies of the electric or mechanical part of the combined system, comprising the wind farm and the network, and the frequency of the exchanged energy is below the fundamental frequency of the system. This phenomenon may cause severe damage in the wind farm, if not prevented [22]–[24].

In order to address the SSR problem in DFIG-based wind farm, this paper studies SSR damping in DFIG-based wind farms by designing an SSRDC using residue-based analysis and root-locus diagrams. Three signals are tested as ICS including rotor speed, transmission line real power, and voltage across the series capacitor, and the optimum ICS is identified using both residue-based analysis and root-locus method. Moreover, several possible points of the rotor-side converter (RSC) and grid-side converter (GSC) controllers of the DFIG wind farm, where the SSRDC can be introduced, are studied and the optimum points are identified.

The SSR damping using DFIG-based wind farms has also been studied by Fan and Miao in [25]. Their goal is to design an auxiliary SSRDC for the GSC controllers using eigenvalue analysis method in order to increase the stability of both subsynchronous and supersynchronous (SupSR) modes. Only averaged converter models are used for validation. The novel contribution of the current work over [25] can be summarized as follows.

Manuscript received May 05, 2014; revised September 02, 2014 and November 21, 2014; accepted December 08, 2014. This work was supported by the National Science Foundation (NSF) I/UCRC (Industry/University Cooperative Research Center) for Grid-Connected Advanced Power Electronic Systems (GRAPES) Center, under Grant 1439689. Paper no. TSTE-00205-2014.

The authors are with the Department of Electrical Engineering, University of South Carolina, Columbia, SC 29208 USA (e-mail: Mohammah@email.sc.edu; Santi@cec.sc.edu).

Color versions of one or more of the figures in this paper are available online at http://ieeexplore.ieee.org.

Digital Object Identifier 10.1109/TSTE.2014.2380782

1) All different points of the RSC and GSC are tested in order to find the optimal point to insert the SSRDC.
2) The discussions presented based on small-signal stability and eigenvalue analysis in MATLAB/Simulink are validated using detailed time-domain simulations in power system computer aided design/ electromagnetic transients including dc (PSCAD/EMTDC), including converter switching models.
3) Using both eigenvalue analysis and time-domain simulations, it is shown why the RSC cannot be used as a potential insertion point for the SSRDC.
4) It is shown that the improper selection of the input control signal (ICS) to the SSRDC may not only result in unstable SupSR mode but also can make other system modes, such as electromechanical and shaft modes, unstable.
5) Two methods are discussed to derive the optimal ICS to the SSRDC, and the methods are validated using time-domain simulations.

This paper is organized as follows. In Section II, the studied power system and its small-signal stability modeling is briefly described. In Section III, the SSR phenomenon in fixed series-compensated DFIG is briefly presented. In this section, time-domain simulation in PSCAD/EMTDC is also presented to verify the eigenvalue analysis. In Section IV, the RSC and GSC controllers of DFIG used in this paper are described. In Section V, an SSRDC is designed using residue-based and root-locus methods. Using these two methods, the optimum point within the DFIG converter where to insert the SSRDC and optimum ICS to the SSRDC are identified. The optimum converter and ICS should enable the SSRDC to damp the SSR mode using a simple proportional gain, without destabilizing other system modes. The proportional controller is chosen, over other options, such as lead-lag compensators and state compensators, for its simplicity and for the fact that the root-locus method can be used for determining the proportional gain value. More complex compensators have a larger number of parameters and tend to require trial-and-error parameter tuning, which is time-consuming and undesirable. In Section VI, the effectiveness of the SSRDC design process is validated using time-domain simulations in PSCAD/EMTDC. In Section VII, two methods are discussed to locally estimate the ICS. Finally, Section VII concludes this work.

II. Power System Description

The studied power system, shown in Fig. 1, is adapted from the IEEE first benchmark model (FBM) for SSR studies [22]. In this system, a 100-MW DFIG-based offshore wind farm is connected to the infinite bus via a 161-kV series-compensated transmission line [26], [27]. The 100-MW wind farm is an aggregated model of 50 wind turbine units, where each unit has a power rating of 2 MW. In fact, a 2-MW wind turbine is scaled-up to represent the 100-MW wind farm. This simplification is supported by several studies [12], [28] showing that an aggregated wind farm model is adequate for power system dynamics studies.

The differential equations for eigenvalue analysis are obtained directly using the parameters of the system. Detailed modal analysis of the power system modes have been described in the authors' previous research in [29] and [30]. A sixth-order model is used to represent the induction generator (IG) stator and rotor current dynamics, whereas a third-order model is used to represent the shaft system. The high-frequency switching dynamics of the GSC and RSC are neglected in the dynamic modeling process, but both the inner and the outer control loops of RSC and the GSC are modeled in this paper. The dynamics of the dc link between RSC and GSC are also considered, which is represented by first-order differential equations. Additionally, a fourth-order model is considered for the series-compensated transmission line. Thus, the complete system model is of 22nd order.

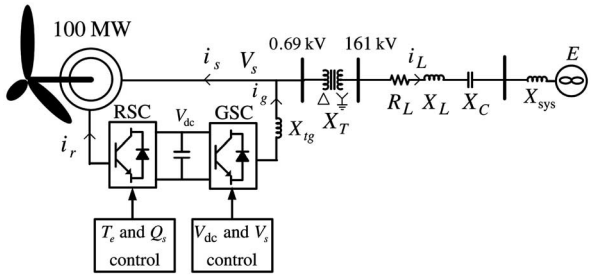

Fig. 1. One line diagram of the studied power system. R_L, transmission line resistance; X_L, transmission line reactance; X_T, transformer reactance; $X_{\rm sys}$, system impedance; X_C, fixed series capacitor; X_{tg}, transformer reactance in GSC; V_s, generator's terminal voltage; i_L, line current; i_g, GSC current; i_s, stator current; and i_r, rotor current [2], [22].

III. SSR Analysis in Series-Compensated DFIG

A series-compensated power system with a compensation level defined as $K = \frac{X_C}{\sum X}$ excites subsynchronous currents at a frequency given by [21]

$$f_n = f_s \sqrt{\frac{X_C}{\sum X}} \tag{1}$$

where $\sum X$ is the entire reactance seen from infinite bus, f_n is the natural frequency of the electric system, and f_s is the fundamental frequency of the system.

At this frequency, the slip, given by (2), becomes negative since the natural resonance frequency f_n is less than the electrical frequency corresponding to the generator rotor speed f_r

$$S = \frac{f_n - f_r}{f_n}. \tag{2}$$

If the magnitude of the equivalent rotor resistance, i.e., $\frac{R_r}{S} < 0$, exceeds the sum of the resistances of the armature and the network, there will be an equivalent negative resistance at the subsynchronous frequency, and the subsynchronous current would increase with time. This phenomenon is called induction generator effect (IGE) [21] and only involves rotor electrical dynamics [21].

A. System Modes and Participation Factor

Table I shows the eigenvalues of the system when the wind speed is 7 m/s and the compensation level is 55%. In Table I,

TABLE I
EIGENVALUES OF THE SYSTEM AT 55% SERIES COMPENSATION AND 7 m/s WIND SPEED

Mode	Eigenvalue	Mode	Eigenvalue
$\lambda_{1,2}$	**+1.2126** ± j128.5545	λ_{15}	–113.5742
$\lambda_{3,4}$	–5.2253 ± j620.3963	λ_{16}	–0.5000
$\lambda_{5,6}$	–10.9322 ± j100.0909	λ_{17}	–0.01392
$\lambda_{7,8}$	–0.9974 ± j5.9965	λ_{18}	–0.0028
$\lambda_{9,10}$	–859.1914 ± j4219.9308	λ_{19}	–19.9297
$\lambda_{11,12}$	–0.1178 ± j0.5332	λ_{20}	–20.8000
λ_{13}	–2181.4727	λ_{21}	–0.0000
λ_{14}	–97.6980	λ_{22}	–0.0000

TABLE II
PARTICIPATION FACTORS AT 55% SERIES COMPENSATION AND 7 m/s WIND SPEED

	$\lambda_{1,2}$	$\lambda_{3,4}$	$\lambda_{5,6}$	$\lambda_{7,8}$	$\lambda_{9,10}$
q-axis stator current-i_{qs}	**0.2791**	**0.2210**	**0.2783**	0.0031	**0.3435**
d-axis stator current-i_{ds}	**0.2081**	**0.1755**	**0.2057**	0.0971	0.09770
q-axis rotor current-i_{qr}	**0.2790**	**0.2027**	**0.2907**	0.0034	**0.1319**
d-axis rotor current-i_{dr}	**0.2082**	**0.1610**	**0.2172**	**0.1117**	0.0830
q-axis cap. voltage-v_{Cq}	0.0069	0.0671	0.0016	0.0030	0.0003
d-axis cap. voltage-v_{Cd}	0.0066	0.0689	0.0015	0.0000	0.0000
q-axis line current-i_{Lq}	0.0050	0.0487	0.0014	0.0000	0.0717
d-axis line current-i_{Ld}	0.0056	0.0544	0.0017	0.0056	0.0051
Rotor speed-$\bar{\omega}_r$	0.0007	0.0000	0.0015	**0.3097**	0.0000
Turbine speed-$\bar{\omega}_m$	0.0000	0.0000	0.0000	0.0668	0.0000
Torque between masses T_{tg}	0.0000	0.0000	0.0000	**0.3849**	0.0000
DC-link voltage-v_{DC}	0.0000	0.0002	0.0000	0.0000	**0.2613**

eigenvalues λ_{13} to λ_{22} represent nonoscillatory stable modes. Furthermore, complex conjugate eigenvalues $\lambda_{11,12}$ are related to the PI regulators.

Participation factor is a measure of the relative participation of jth state variable in the ith mode of the system. The magnitude of the normalized participation factors for an eigenvalue λ_i is defined as [31]

$$P_{ji} = \frac{|\Phi_{ji}||\Psi_{ij}|}{\sum_{k=1}^{n} |\Phi_{ki}||\Psi_{ik}|} \tag{3}$$

where P_{ji} is the participation factor, n is the number of modes or state variables, Φ is the right eigenvector, and Ψ is the left eigenvector.

Table II shows the participation factors of the system modes of interest when the wind speed is 7 m/s and the compensation level is 55%. In this table, larger participation factors in each column are bold. By looking at this table, one can readily find the participation of each state variable in system modes. Based on Table II and using participation factors related to $\lambda_{9,10}$, one can see that this mode is associated primarily to the q-axis stator current i_{qs}, the q-axis rotor current i_{dr}, and the dc-link voltage $v_{\rm dc}$.

Through examination of participation factor analysis and the actual frequencies of the system modes, $\lambda_{5,6}$ and $\lambda_{7,8}$ are identified to be the electro-mechanical mode and the shaft mode, respectively. Eigenvalues $\lambda_{1,2}$ with the oscillating frequency 20.46 Hz and $\lambda_{3,4}$ with the oscillating frequency 98.74 Hz are the SSR and SupSR modes, respectively. Table I also shows that the SSR mode at 55% compensation and 7 m/s wind speed is unstable, as the real part of this mode is positive.

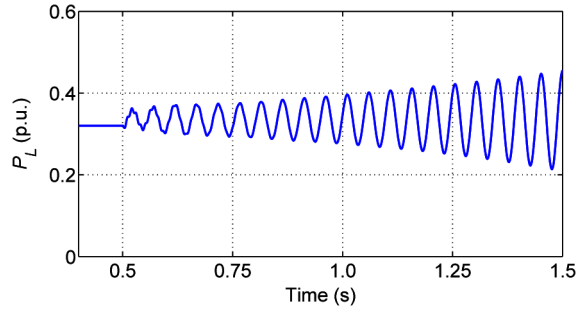

Fig. 2. Transmission line real power P_L at 55% compensation level and 7 m/s wind speed.

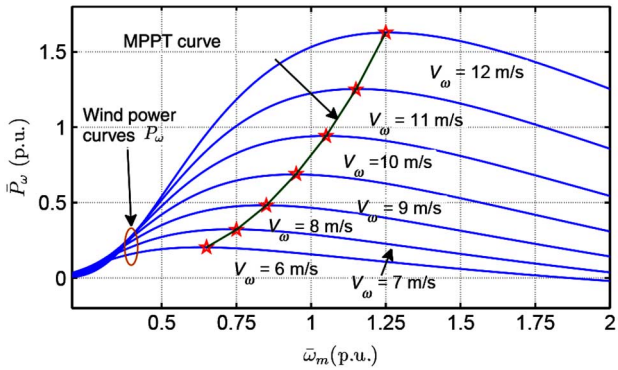

Fig. 3. Wind power $\bar{P}_\omega$ (p.u.), wind turbine shaft speed $\bar{\omega}_m$ (p.u.), and wind speed V_ω (m/s) relationship.

B. Time-Domain Simulation

In order to confirm the eigenvalue analysis provided in Table I, time-domain simulation is also presented. Fig. 2 shows real power of the transmission line when the series compensation is 55% and the wind speed is 7 m/s. Note that in the given simulation result, the system is first started with a series compensation level, i.e., 50% at which the wind farm is stable, and then at $t = 0.5$ s, the compensation level is changed. As this figure shows, as we expected from Table I, the system is unstable, and the oscillating frequency is about 20.45 Hz, which matches well with what is calculated in Table I using modal analysis ($\frac{128.5545}{2\pi} = 20.46$ Hz).

IV. DFIG CONVERTER CONTROLLERS

In order to achieve high efficiency in the DFIG wind farm, the maximum power point tracking (MPPT) is used [32]. Fig. 3 shows the wind power versus wind turbine shaft speed in per unit for various wind speeds with the indication of MPPT curve. To enforce operation on the MPPT curve, for a given wind speed V_ω, the optimum reference power and optimum rotational speed are obtained. The GSC and RSC are designed to enable the DFIG to work on the MPPT curve. Figs. 4 and 5 show the block diagrams of the two controllers, respectively. In this paper, the RSC controller is responsible for regulating the electric torque T_e and stator reactive power Q_s. Moreover, the GSC is responsible for controlling the dc-link voltage $V_{\rm dc}$ and the IG terminal voltage V_s.

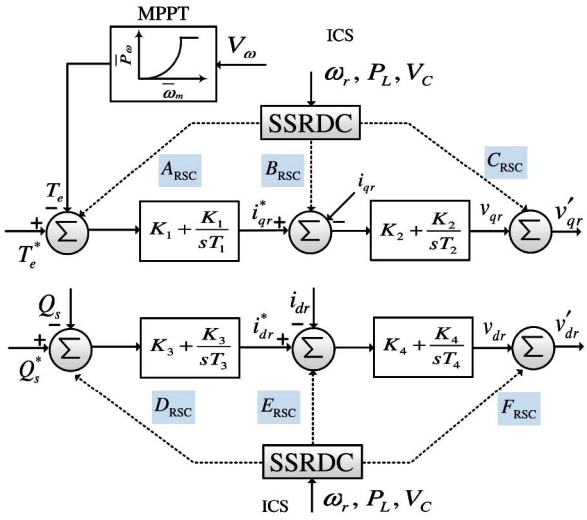

Fig. 4. RSC controllers.

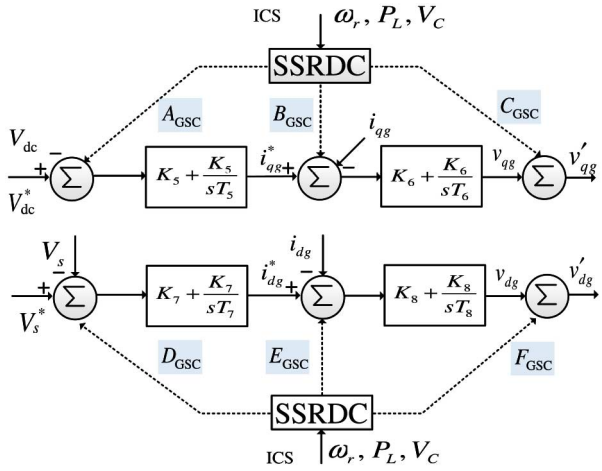

Fig. 5. GSC controllers.

The SSR damping is achieved using an additional SSRDC on either the GSC or RSC, operating on a single ICS as illustrated in Figs. 4 and 5. The SSRDC block is represented in Fig. 6, which is based on proportional gain $K_{\rm SSR}$ and washout filter. The value of the $K_{\rm SSR}$ for each ICS is obtained using root-locus method, such that 6% damping ratio is obtained for the SSR mode. The 6% damping ratio is chosen arbitrarily, but the procedure can be used for any desired value of damping ratio. Moreover, a washout filter, which is a high-pass filter, is included in the SSRDC block to eliminate the effect of the SSRDC on the steady-state operating condition. Usually, the value of the washout filter time constant T_w is chosen to be between 5 and 10 s. In this paper, $T_w = 5$ s. [31].

There are a variety of options for the ICS, as shown in Figs. 4 and 5. In this paper, rotor speed ω_r, transmission line real power P_L, and voltage across the series compensation V_C are examined, and the optimum ICS is identified with the help of residue-based analysis and root-locus diagrams, as explained in the next section.

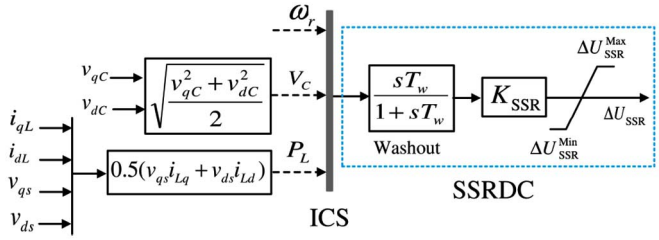

Fig. 6. SSRDC block diagram.

V. ICS and Converter Selection for SSRDC Design

In this section, using residue-based analysis and root-locus method, an optimum ICS to the SSRDC is introduced. The optimum ICS should enable the SSRDC to damp the SSR without decreasing or destabilizing the other system modes. The SSRDC can be inserted at different points of the RSC and GSC controllers, identified as $A_{\rm RSC}$–$F_{\rm RSC}$ and $A_{\rm GSC}$–$F_{\rm GSC}$ in Figs. 4 and 5. These insertion points are examined to find out where the SSRDC could be introduced.

A. Residue-Based Analysis for Identification of Optimum ICS

The state-space model and transfer function of a single-input single-output are defined as [31]

$$\dot{X} = AX + BU \tag{4}$$

$$Y = CX \tag{5}$$

where A, B, and C are the state matrix, the control matrix, and the output matrix, respectively.

The transfer function G(s) can be factored as given in (6)

$$G(s) = C(SI - A)^{-1}B = \frac{Y(s)}{U(s)} = \sum_{i=1}^{n} \frac{R_i}{s - \lambda_i} \tag{6}$$

where $\lambda_1 \ldots \lambda_n$ are the n eigenvalues and $R_1 \ldots R_n$ are the corresponding residues.

For a complex eigenvalue λ_i, the residue R_i is also a complex number and can be expressed as [31]

$$R_i = C\Phi_i\Psi_i B \tag{7}$$

where Φ_i and Ψ_i are right and left eigenvectors, respectively.

The residue can be considered as a vector having a certain direction. If the magnitude of the residue is large enough, then a smaller gain is needed for the feedback control system. Furthermore, the angle of the residue could determine the location of the closed-loop pole in root-locus diagram.

B. Analysis of Rotor Speed (ω_r) as ICS

Table III shows the residues of the SSR, SupSR, electromechanical, and shaft modes when ω_r is used as ICS and SSRDC is implemented at different points of the RSC and GSC controllers, identified in Figs. 4 and 5 as $A_{\rm RSC}$–$F_{\rm RSC}$ and

TABLE III
RESIDUE OF THE SSR AND SUPSR, ELECTRO-MECHANICAL, AND SHAFT MODES AT $V_\omega = 7$ m/s AND $K = 55\%$: ω_r AS ICS

$V_\omega = 7$ m/s $- K = 55\%$	ω_r as ICS			
	SSR mode	SupSR mode	Elec. mech. mode	Shaft mode
A_{RSC}	$5.7922e^{-11}\angle 55.4^o$	$4.2400e^{-13}\angle -107.2^o$	$9.7227e^{-11}\angle -152.6^o$	$2.9204e^{-10}\angle -156.5^o$
B_{RSC}	$5.7152e^{-7}\angle 64.3^o$	$4.2389e^{-9}\angle -105.4^o$	$9.7406e^{-7}\angle -141.2^o$	$8.9096e^{-7}\angle -74.6^o$
C_{RSC}	$3.0766\angle -57.4^o$	$0.0387\angle 102.5^o$	$4.5807\angle 107.6^o$	$0.2223\angle -154.6^o$
D_{RSC}	$1.0653e^{-7}\angle -57.9^o$	$4.1038e^{-10}\angle 134.7^o$	$1.8556e^{-7}\angle 93.4^o$	$6.0627e^{-6}\angle -176.1^o$
E_{RSC}	$0.0010\angle -40.6^o$	$4.0975e^{-6}\angle 138.4^o$	$0.0017\angle 115.8^o$	$.0093\angle -85.4^o$
F_{RSC}	$3.1042\angle 30.9^o$	$0.0381\angle 174.4^o$	$4.5029\angle -162.2^o$	$1.4504\angle 13.1^o$
A_{GSC}	$4.6968e^{-5}\angle -57.7^o$	$0.0001\angle 111.8^o$	$4.6674e^{-5}\angle -95.8^o$	$6.8484e^{-6}\angle -67.1^o$
B_{GSC}	$0.0007\angle -57.5^o$	$0.0012\angle 113.4^o$	$0.0001\angle -95.5^o$	$6.9265e^{-5}\angle -62.4^o$
C_{GSC}	$0.0006\angle -19.8^o$	$0.0012\angle 121.1^o$	$0.0001\angle -47.6^o$	$4.2303e^{-6}\angle 33.4^o$
D_{GSC}	$0.0059\angle -83.8^o$	$0.0010\angle 73.7o$	$0.0007\angle 116.6^o$	$0.0008\angle 115.4^o$
E_{GSC}	$0.0593\angle -83.6^o$	$0.0104\angle 73.8^o$	$0.0077\angle 116.9^o$	$0.0075\angle 120.1^o$
F_{GSC}	$0.0466\angle -45.9^o$	$0.0105\angle 82.9^o$	$0.0058\angle 164.8^o$	$0.0004\angle -143.8^o$

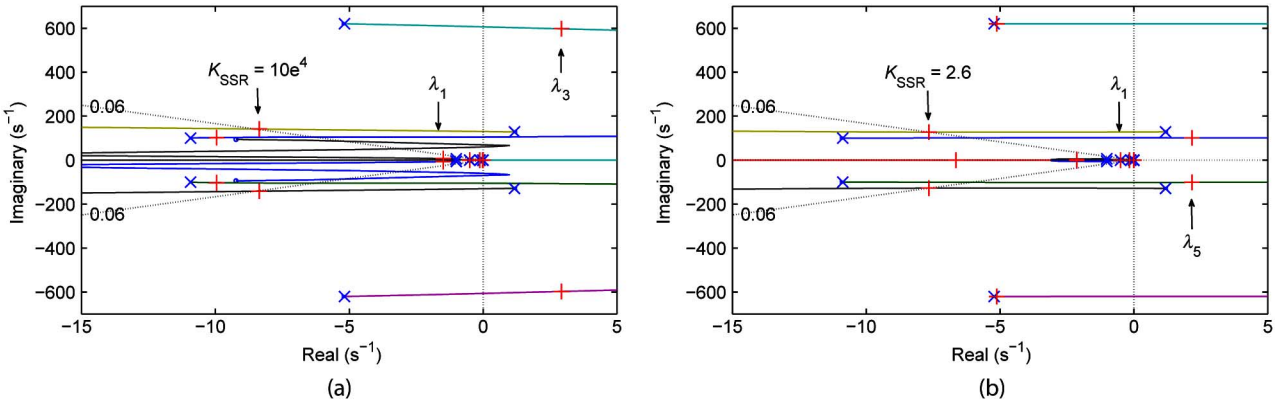

Fig. 7. Root-locus diagram with ω_r as ICS with SSRDC implemented: (a) in GSC controller at point A_{GSC} and (b) in RSC controller at point F_{RSC}.

A_{GSC}–F_{GSC}, respectively. From this table, it is observed that with the SSRDC implemented at points A_{RSC}, B_{RSC}, D_{RSC}, or A_{GSC}, a very large gain is needed to move the SSR mode from the right-half plane (RHP) to the left-half plane (LHP), since the magnitude of the SSR residues for these points is very small. Moreover, due to the opposing directions of these modes, at high gain, the stability of other system modes may decrease or even destabilize the system.

These shortcomings are visualized using root-locus diagram shown in Fig. 7(a), where SSRDC with ω_r as ICS is implemented at point A_{GSC}. Note that $\times$ and $+$ signs in the root-locus diagrams shown in this paper indicate the open-loop and closed-loop system poles, respectively. As seen in Fig. 7(a), a very large SSR gain, i.e., $K_{\text{SSR}} = 10e^4$, can yield the desired 6% damping ratio for the SSR mode; however, the SupSR mode becomes unstable for this gain. Therefore, this signal cannot be used as ICS at points A_{RSC}, B_{RSC}, D_{RSC}, or A_{GSC}.

Using ω_r as the ICS and placing the controller at the remaining points, the smaller gain necessary to stabilize the SSR mode still causes destabilization of the non-SSR modes. This occurs because the residues of the SSR mode do not have the same polarity as the residues of the other modes, as should be clear from Table III. For example, at point C_{RSC}, the residue of the SSR mode has opposite polarity compared to all residues of the other modes given in Table III. Conversely, when taking F_{RSC} as the control point, stabilizing the SSR mode will result in decreasing the stability of the SupSR mode and the electro-mechanical mode. The root locus for this control point, shown in Fig. 7(b), shows that as the SSR mode moves to the left and becomes stable, the SupSR and the electro-mechanical modes move to the right. In particular, the electro-mechanical mode becomes unstable first, whereas the SupSR mode moves only by a small amount. This was to be expected given the larger amplitude of the electro-mechanical mode residue (4.5029) compared to the SupSR mode residue (0.0381).

C. Analysis of Transmission Line Real Power (P_L) as ICS

Table IV shows the residues of the SSR, SupSR, electro-mechanical, and shaft modes when P_L is used as ICS and the SSRDC is implemented at different points of RSC and GSC controllers. As seen in this table, implementation of the SSRDC at points A_{RSC}, B_{RSC}, and D_{RSC} will require a very large gain to move the SSR mode from RHP to LHP since the magnitude of the SSR residues is very small. Moreover, even if this large gain is provided, the residues of the SSR mode are in opposite direction with the residues of the SupSR, electro-mechanical, and shaft modes, and therefore, it is expected that with an

TABLE IV
RESIDUE OF THE SSR AND SUPSR, ELECTRO-MECHANICAL, AND SHAFT MODES AT $V_\omega = 7$ m/s AND $K = 55\%$: P_L AS ICS

$V_\omega = 7$ m/s $- K = 55\%$	I_L as ICS			
	SSR mode	SupSR mode	Elec. mech. mode	Shaft mode
A_{RSC}	$9.8321e^{-9}\angle -33.5^o$	$3.4496e^{-10}\angle 158.3^o$	$1.2827e^{-8}\angle 125.7^o$	$4.5664e^{-10}\angle -148.8^o$
B_{RSC}	$9.7013e^{-5}\angle -24.6^o$	$3.4484e^{-6}\angle 160.1^o$	$0.0001\angle 137.1^o$	$1.3930e^{-6}\angle -66.9^o$
C_{RSC}	$522.2481\angle 32.6^o$	$31.5041\angle -171.8^o$	$604.3783\angle -154.6^o$	$0.3480\angle 32.9^o$
D_{RSC}	$1.7985e^{-5}\angle 32.1^o$	$3.3388e^{-7}\angle -139.6^o$	$2.4572e^{-5}\angle -168.7^o$	$9.4786e^{-6}\angle 11.1^o$
E_{RSC}	$0.1712\angle 49.3^o$	$0.0033\angle -135.9^o$	$0.2373\angle -146.3^o$	$0.0146\angle 101.8^o$
F_{RSC}	$524.7688\angle 121.1^o$	$31.0048\angle -99.9^o$	$594.4558\angle -64.5^o$	$2.2687\angle -159.5^o$
A_{GSC}	$0.0131\angle 33.2^o$	$0.0974\angle -162.5^o$	$0.0027\angle 2.5^o$	$1.2946e^{-5}\angle 120.4^o$
B_{GSC}	$0.1315\angle 33.4^o$	$0.9746\angle -162.4^o$	$0.0261\angle 2.8^o$	$0.0001\angle 125.1^o$
C_{GSC}	$0.1033\angle 71.1^o$	$0.9634\angle -153.2o$	$0.0196\angle 50.7^o$	$8.01651e^{-6}\angle -138.8^o$
D_{GSC}	$1.0082\angle 7.1^o$	$0.8667\angle 159.3^o$	$0.1019\angle -144.9^o$	$0.0011\angle -56.8^o$
E_{GSC}	$10.0817\angle 7.3^o$	$8.6672\angle 159.4o$	$1.0198\angle -144.6^o$	$0.0118\angle -52.1^o$
F_{GSC}	$7.9216\angle 45.0^o$	$8.5681\angle 168.5^o$	$0.7664\angle -96.7^o$	$0.0007\angle 43.8^o$

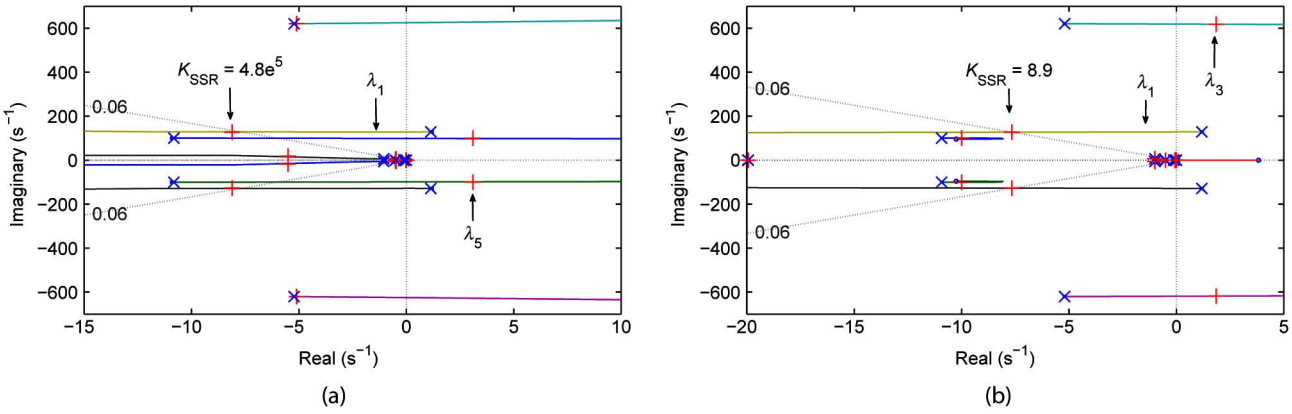

Fig. 8. Root-locus diagram with P_L as ICS with SSRDC implemented in: (a) RSC controller at point D_{RSC} and (b) GSC controller at point D_{GSC}.

increasing SSR gain, the other modes will move in opposite directions.

This is evident from the root-locus diagram shown in Fig. 8(a), where SSRDC with P_L as ICS is implemented at point D_{RSC}. As seen in this figure, although the SSR mode becomes stable with a very large gain, i.e., $K_{\text{SSR}} = 4.8e^5$, this makes the electro-mechanical mode unstable. Moreover, the SupSR mode has a tendency to move to the RHP with increasing the SSR gain. Therefore, this signal cannot be implemented as ICS at points A_{RSC}, B_{RSC}, and D_{RSC}.

For the other points of RSC and GSC controllers, i.e., C_{RSC} through F_{RSC}, and A_{GSC} through F_{GSC}, if P_L is used as ICS, a smaller SSR gain will be needed to move the SSR mode from RHP to LHP, since the magnitude of the SSR residues are larger compared to the previous case. However, stabilizing the SSR mode in these cases will result in decreasing the stability, or even destabilizing the other system modes. This is because, the residues of the SSR mode do not have the same polarity as the other modes, as shown in Table IV. For example, at point F_{RSC}, the residue of the SSR mode has opposite polarity compared to SupSR and electro-mechanical modes, as seen in Table IV.

As another example, with SSRDC implemented at point D_{GSC}, stabilizing the SSR mode deteriorates the stability of SupSR and electro-mechanical modes. Fig. 8(b) represents the root-locus diagram of the system for this case. As shown in this figure, to have a 6% damping ratio for the SSR mode, a small SSR feedback gain, i.e., $K_{\text{SSR}} = 8.9$, is needed; however, this can result in destabilizing the SupSR mode. Therefore, regardless of the chosen insertion point for the SSRDC, the line real power P_L is not a good choice for ICS and should not be used.

D. Analysis of Capacitor Voltage (V_C) as ICS

Table V shows the residues of the SSR, SupSR, electro-mechanical, and shaft modes when V_C is used as ICS and the SSRDC is implemented at different points of RSC and GSC controllers. As seen in this table, the implementation of SSRDC at points A_{RSC}, B_{RSC}, and D_{RSC} will require a very large gain to move the SSR mode from RHP to LHP since the magnitude of the SSR residues is very small. Moreover, even if this large gain is provided to move the SSR mode to the LHP—since according to Table V, the residues of the SSR mode at these points are in opposite direction with the residues of the electro-mechanical mode—it is expected that with an increasing SSR gain, the electro-mechanical mode will be destabilized.

For the other points of the RSC, i.e., C_{RSC}, E_{RSC}, and F_{RSC}, even if the magnitude of the SSR residues corresponding to these points is large, stabilizing the SSR mode in these cases will also result in decreasing the stability, or even destabilizing the electro-mechanical mode, as the residues of the SSR

TABLE V
RESIDUE OF THE SSR AND SUPSR, ELECTRO-MECHANICAL, AND SHAFT MODES AT $V_\omega = 7$ m/s AND $K = 55\%$: V_C AS ICS

$V_\omega = 7$ m/s $- K = 55\%$	V_C as ICS			
	SSR mode	SupSR mode	Elec. mech. mode	Shaft mode
A_{RSC}	$5.8808e^{-9}\angle -38.7^o$	$2.1628e^{-10}\angle -22.1^o$	$6.9276e^{-9}\angle 125.8^o$	$1.3344e^{-10}\angle -140.2^o$
B_{RSC}	$5.7765e^{-5}\angle -29.8^o$	$2.1623e^{-6}\angle -20.3^o$	$6.9392e^{-5}\angle 137.1^o$	$4.0756e^{-7}\angle -58.3^o$
C_{RSC}	$312.0201\angle 27.3^o$	$19.7537\angle 7.6^o$	$327.2719\angle -154.5^o$	$0.1016\angle 41.5^o$
D_{RSC}	$1.0752e^{-5}\angle 26.9^o$	$2.0934e^{-7}\angle 39.8^o$	$1.3257e^{-5}\angle -168.7^o$	$2.7709e^{-6}\angle 20.1^o$
E_{RSC}	$0.1023\angle 44.1^o$	$0.0020\angle 43.5^o$	$0.1281\angle -146.3^o$	$0.0042\angle 110.7^o$
F_{RSC}	$313.2\angle -64.9^o$	$19.4\angle -100.4^o$	$321.7\angle 114.7^o$	$0.6629\angle 28.9^o$
A_{GSC}	$0.0078\angle 27.2^o$	$0.0611\angle 16.9^o$	$0.0014\angle 1.8^o$	$3.8819e^{-6}\angle 128.9^o$
B_{GSC}	$0.0783\angle 27.4^o$	$0.6110\angle 17.0^o$	$0.0141\angle 2.1^o$	$133.6e^{-5}\angle 140.2^o$
C_{GSC}	$0.0615\angle 65.1^o$	$0.6041\angle 26.2^o$	$0.01061\angle 50.0^o$	$2.3978e^{-6}\angle -122.9^o$
D_{GSC}	$0.6003\angle 12.5^o$	$0.6238\angle 2.4^o$	$0.2137\angle 30.5^o$	$0.0014\angle -10.1^o$
E_{GSC}	$4.5777\angle 12.8^o$	$6.2381\angle 2.4^o$	$2.1396\angle 30.8^o$	$0.0144\angle -18.4^o$
F_{GSC}	$3.1982\angle 52.6^o$	$6.1732\angle 11.2^o$	$1.6500\angle 84.8^o$	$0.0008\angle -27.6^o$

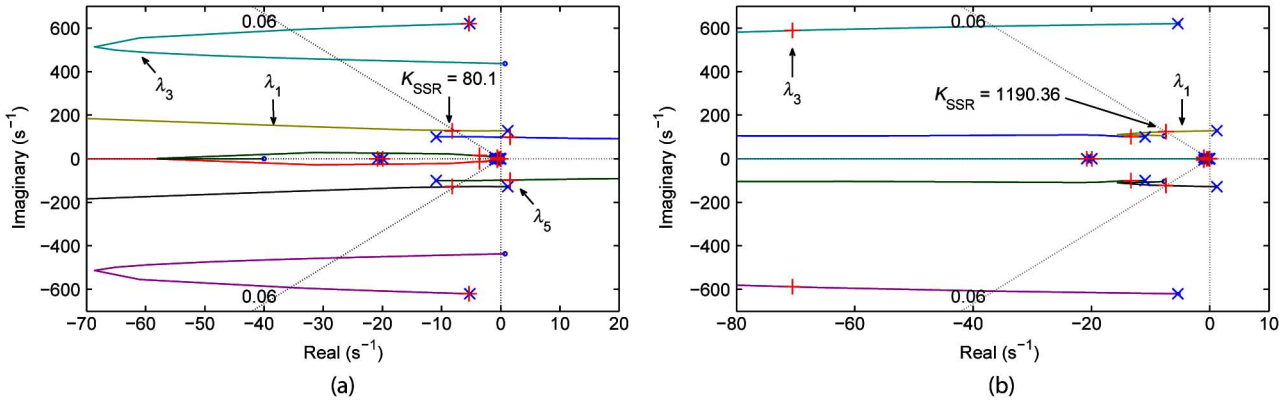

Fig. 9. Root-locus diagram with V_C as ICS with SSRDC implemented in: (a) RSC controller at point E_{RSC} and (b) GSC controller at point A_{GSC}.

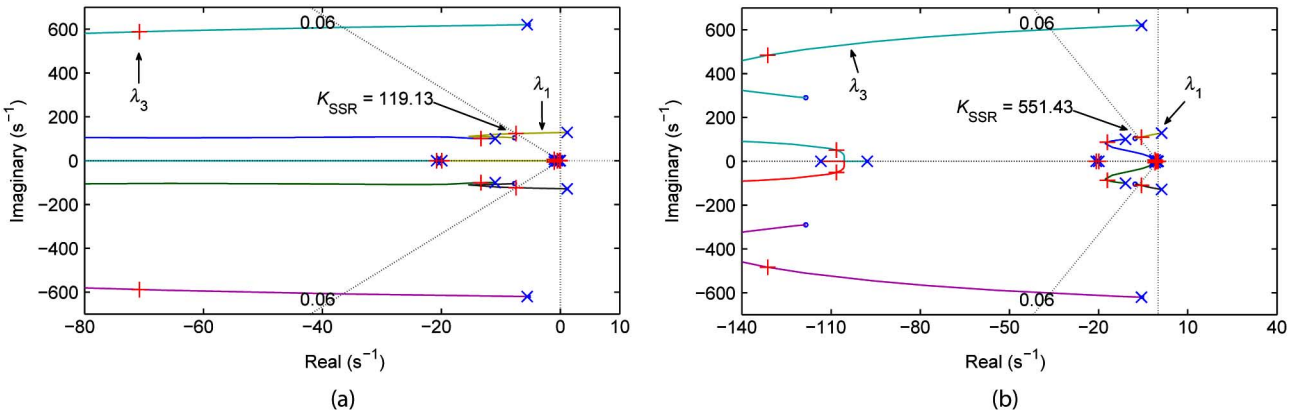

Fig. 10. Root-locus diagram with V_C as ICS with SSRDC implemented in GSC controller at point: (a) B_{GSC} and (b) C_{GSC}.

mode and electro-mechanical mode point in opposite directions. This should be readily apparent upon examination of the root-locus diagram, shown in Fig. 9(a), where the SSRDC with V_C as ICS is implemented at point E_{RSC}. As seen in this figure, although the damping ratio of the SSR mode becomes 6% with $K_{\mathrm{SSR}} = 80.1$, this makes the electro-mechanical mode unstable. In conclusion, all controller insertion points on the RSC are not viable.

However, when implementing the SSRDC at GSC controller points, i.e., A_{GSC} through C_{GSC}, except the residues of the shaft mode, all other residues point at the same direction with the residues of the SSR mode, as seen in Table V. This shows that stabilizing the SSR mode by increasing the SSR gain can also increase the stability of the SupSR mode and electro-mechanical mode. This operation may destabilize the shaft mode, though this destabilization will not happen due to the much smaller magnitude of the residues of this mode. Figs. 9(b) and 10(a) and (b) confirm this prediction, stabilizing the SSR mode by increasing the SSR gain has also increased the stability of the SupSR and electro-mechanical

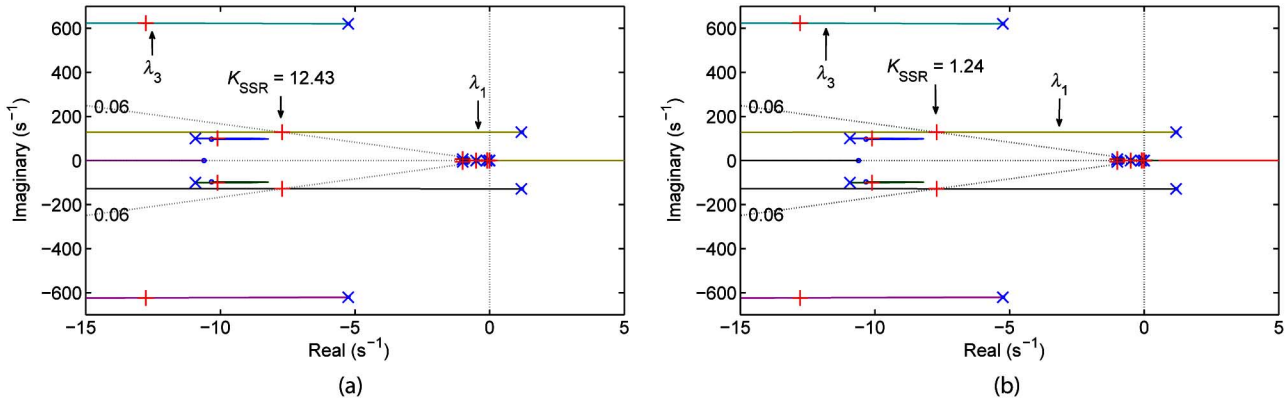

Fig. 11. Root-locus diagram with V_C as ICS with SSRDC implemented in GSC controller at point: (a) $D_{\rm GSC}$ and (b) $E_{\rm GSC}$.

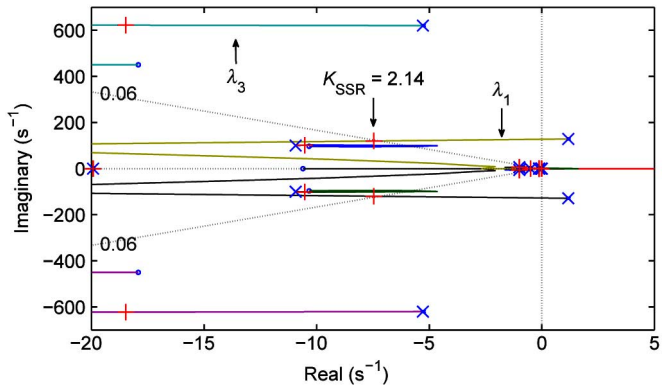

Fig. 12. Root-locus diagram with V_C as ICS with SSRDC implemented in GSC controller at point $F_{\rm GSC}$.

modes. Moreover, no unstable shaft mode was observed by increasing the SSR gain.

For implementation of the SSRDC at points $D_{\rm GSC}$ through $F_{\rm GSC}$, the residues of all modes point at the same direction with that of the SSR mode, as seen in Table V. This shows that by increasing the SSR gain, not only the SSR mode will be stabilized, but also this will increase the stability of all other three modes. Moreover, since the residue magnitude of the SSR mode at these points are much larger compared to that of the SSR mode at points $A_{\rm GSC}$ through $C_{\rm GSC}$, a much smaller SSR gain will be required to stabilize the system. Figs. 11(a) and (b) and 12 represent the root-locus diagrams of the system for the points $D_{\rm GSC}$ through $F_{\rm GSC}$, respectively, where the required SSR feedback gains to have 6% damping ratio for the SSR mode are indicated in these figures. In conclusion, the optimal ICS is the capacitor voltage V_C and the optimal controller insertion points are $D_{\rm GSC}$, $E_{\rm GSC}$, and $F_{\rm GSC}$.

VI. Time-Domain Simulation With SSRDC

To validate the results of Section V, the time-domain simulation of system shown in Fig. 1 with the SSRDC is presented. PSCAD/EMTDC is used to perform the simulations. In the entire simulation, results given in this paper are as follows.

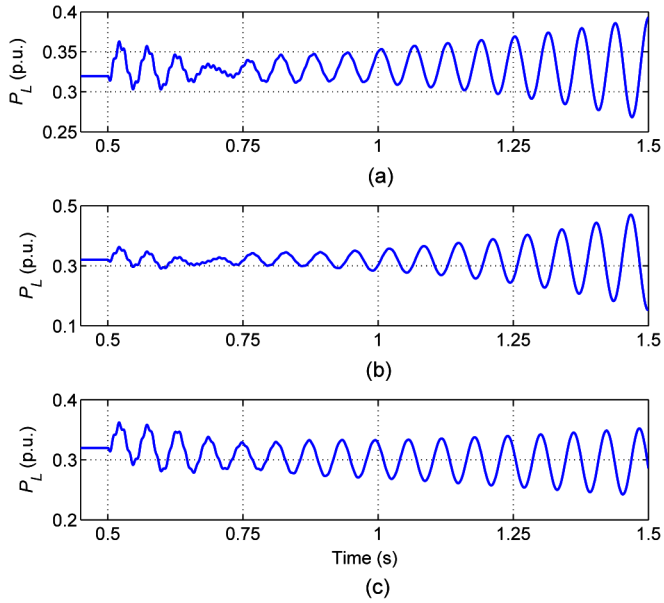

Fig. 13. Dynamic response of the transmission line real power P_L when the SSRDC is implemented at RSC. (a) SSRDC at $F_{\rm RSC}$ with ω_r as ICS. (b) SSRDC at $D_{\rm RSC}$ with P_L as ICS. (c) SSRDC at $E_{\rm RSC}$ with V_C as ICS.

1) Initially, the compensation level is regulated at 50%, where the system is stable, and then at $t = 0.5$ s, the compensation level is changed to 55%, where the system is unstable without SSRDC, due to the SSR mode.
2) The SSRDC gain $K_{\rm SSR}$ in the simulation is obtained using root-locus diagrams, as mentioned before.

A. SSRDC Implemented in RSC Controllers

Fig. 13 shows the dynamic performance of the transmission line real power P_L when the SSRDC is implemented at RSC. Fig. 13(a)–(c) shows that as soon as the compensation level increases from 50% to 55% at $t = 0.5$ s, regardless of which ICS is used, the subsynchronous and SupSR oscillations appear in the transmission line real power, and these oscillations damp out in less than 0.25 s, but another oscillations start to appear in the system dynamics making the wind farm unstable. The frequency of these oscillations is in range of electro-mechanical mode ($\lambda_{5,6}$).

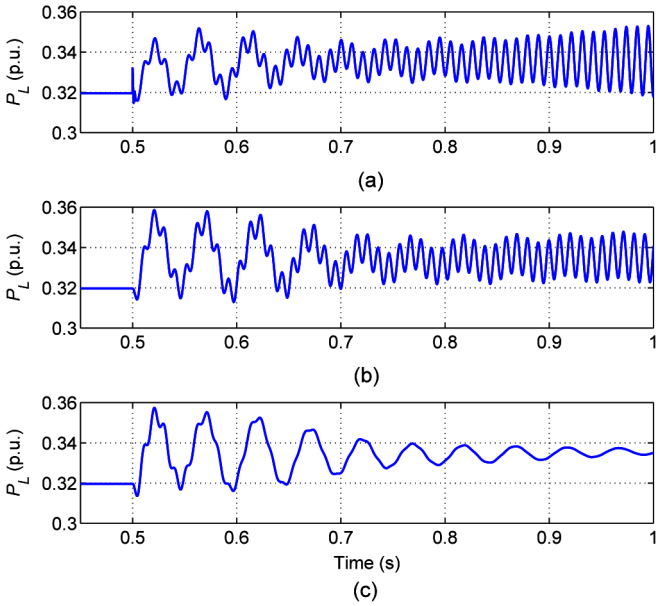

Fig. 14. Dynamic response of the transmission line real power P_L when the SSRDC is implemented at GSC. (a) SSRDC at $A_{\rm GSC}$ with ω_r as ICS. (b) SSRDC at $D_{\rm GSC}$ with P_L as ICS. (c) SSRDC at $D_{\rm GSC}$ with V_C as ICS.

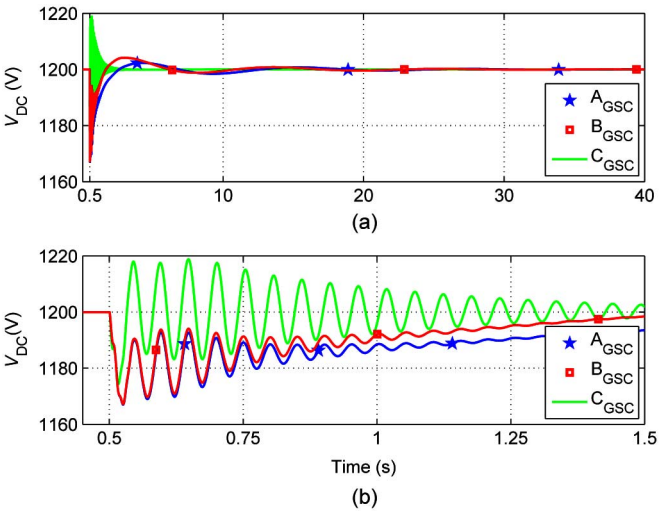

Fig. 15. Dynamic response of the dc link voltage when SSRDC is implemented at $A_{\rm GSC}$, $B_{\rm GSC}$, and $C_{\rm GSC}$. (a) Simulation time from $t = 0.5$ to $t = 40$ s. (b) Simulation time from $t = 0.45$ to $t = 1.5$ s.

Indeed, the reason for the instability of the wind farm in this case is not the SSR mode, but it is the unstable electro-mechanical mode. This was expected from root-locus diagrams shown in Figs. 7(b), 8(a), and 9(a). These root-locus figures clearly show that increasing the SSR gain, to make the SSR mode stable, causes the electro-mechanical mode to go unstable. Therefore, in spite of what kind of ICS is used, the SSRDC cannot be implemented at RSC controllers.

B. SSRDC Implemented in GSC Controllers

Fig. 14(a) and (b) shows the dynamic performance of the transmission line real power P_L when the SSRDC is implemented at GSC with ω_r and P_L as ICSs. Fig. 14(a) and (b)

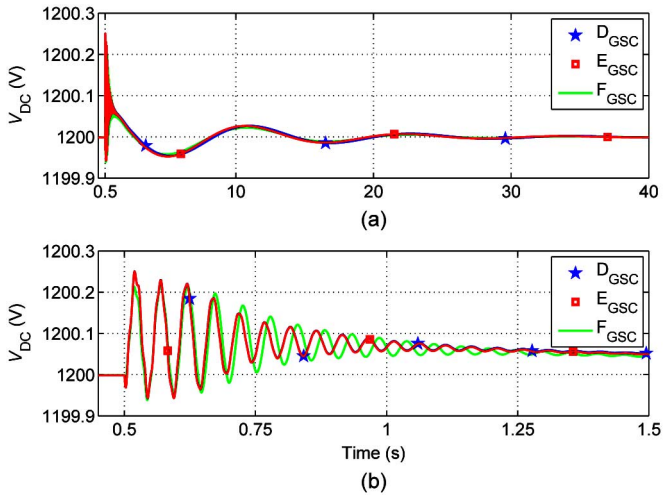

Fig. 16. Dynamic response of the dc link voltage when SSRDC is implemented at $D_{\rm GSC}$, $E_{\rm GSC}$, and $F_{\rm GSC}$. (a) Simulation time from $t = 0.5$ to $t = 40$ s. (b) Simulation time from $t = 0.45$ to $t = 1.5$ s.

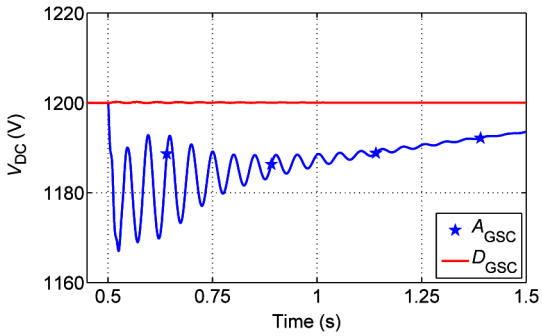

Fig. 17. Dynamic response comparison when SSRDC is implemented at $A_{\rm GSC}$ and $D_{\rm GSC}$.

shows that as soon as the compensation level increases from 50% to 55% at $t = 0.5$ s, the subsynchronous and SupSR oscillations appear in the transmission line real power, but only the former damps out in less than 0.25 s, whereas the latter is sustained in the system and makes the wind farm unstable.

In fact, the reason for the instability of the wind farm, when variables ω_r and P_L are used as ICS, is not the SSR mode, but it is the SupSR mode. This was expected from root-locus diagrams shown in Figs. 7(a) and 8(b). These root-locus figures clearly show that by increasing the SSR gain to make the SSR mode stable, the SupSR mode goes unstable. Therefore, ω_r and P_L cannot be used as ICSs, even when the SSRDC is installed at GSC controllers.

Using V_C as ICS with SSRDC implemented at GSC controllers, on the other hand, can stabilize the wind farm, as illustrated in Fig. 14(c). This was expected from the root-locus diagrams shown in Figs. 9(b)–12.

C. Optimal Point for SSRDC Implementation in GSC Controllers With V_C as ICS

Fig. 15 shows the dc-link voltage $V_{\rm dc}$, when the SSRDC is implemented at points $A_{\rm GSC}$, $B_{\rm GSC}$, and $C_{\rm GSC}$. As seen in

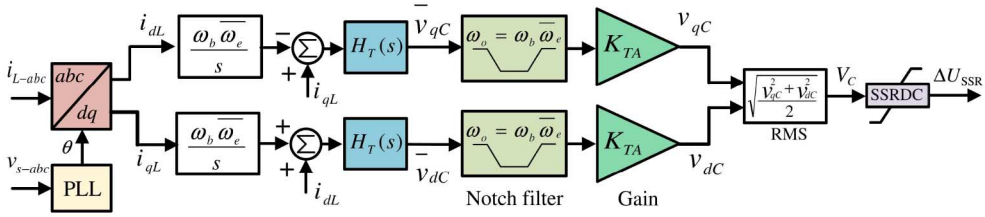

Fig. 18. Derivation of voltage across the series capacitor using qd-axis line currents (Method A).

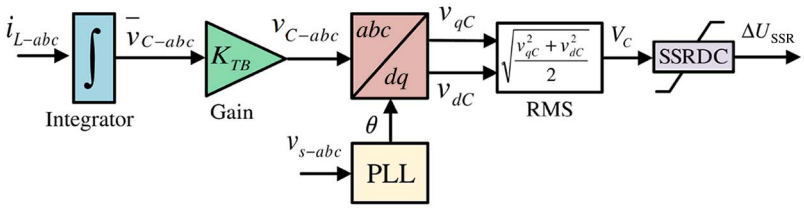

Fig. 19. Derivation of voltage across the series capacitor using instantaneous line current (Method B).

this figure, the SSRDC has successfully damped the SSR mode, and has made the wind farm stable, as expected from root-locus diagrams given in Figs. 9(b) and 10(a) and (b). Fig. 15 shows that implementing the SSRDC at points $A_{\rm GSC}$ and $B_{\rm GSC}$ gives superior performance compared to implementing the SSRDC at $C_{\rm GSC}$ in terms of settling time.

Moreover, Fig. 16 represents the dc-link voltage $V_{\rm dc}$, when the SSRDC is implemented at points $D_{\rm GSC}$, $E_{\rm GSC}$, and $F_{\rm GSC}$ in GSC controllers. As seen in this figure, as expected from root-locus diagrams shown in Fig. 11(a) and (b) and Fig. 12, the SSRDC has successfully attenuated the SSR mode and achieved wind farms stability. Fig. 16 shows that implementing the SSRDC at points $D_{\rm GSC}$ and $E_{\rm GSC}$ brings slightly better performance compared to implementing the SSRDC at points $F_{\rm GSC}$ in terms of settling time. This shows that the SSRDC can interchangeably be implemented at points $D_{\rm GSC}$, $E_{\rm GSC}$, and $F_{\rm GSC}$.

Furthermore, Fig. 17 compares the dc link with the SSRDC implemented at point $A_{\rm GSC}$ and $D_{\rm GSC}$. This figure shows that implementation of the SSRDC at point $D_{\rm GSC}$ causes much less overshoot and settling time in DC link voltage compared to when the SSRDC is implemented at point $A_{\rm GSC}$. This shows that implementation of the SSRDC at $D_{\rm GSC}$, $E_{\rm GSC}$, and $F_{\rm GSC}$ is a better option compared to $A_{\rm GSC}$, $B_{\rm GSC}$, and $C_{\rm GSC}$.

VII. Discussion of Feasibility of Series Capacitor Voltage as ICS

According to the discussion given in this paper, the optimum ICS to the SSRDC is the voltage across the series capacitor, V_C. However, in practical applications of the wind farms, the voltage across the series compensation may not be accessible at the wind turbine for local controls. The question is "can we derive the voltage across the series capacitor using local measurements?" Fortunately, the answer to this question is *Yes*. Here two methods are discussed to derive the V_C from a local measured signal.

A. Derivation From Line Current in $q-d$ (Method A)

The relation between the line current and series capacitor voltage in $q-d$ frame in Fig. 1 is as follows [2], [29]:

$$i_{qL} = \frac{1}{\omega_b X_C}\frac{d}{dt}v_{qC} + \frac{\bar{\omega}_e}{X_C}v_{dC} \tag{8}$$

$$i_{dL} = -\frac{\bar{\omega}_e}{X_C}v_{qC} + \frac{1}{\omega_b X_C}\frac{d}{dt}v_{dC} \tag{9}$$

or in a matrix and Laplace form

$$\begin{bmatrix} i_{qL} \\ i_{dL} \end{bmatrix} = \begin{bmatrix} \frac{1}{\omega_b X_C}s & \frac{\bar{\omega}_e}{X_C} \\ -\frac{\bar{\omega}_e}{X_C} & \frac{1}{\omega_b X_C}s \end{bmatrix} \begin{bmatrix} v_{qC} \\ v_{dC} \end{bmatrix}. \tag{10}$$

Using (10), the series capacitor voltage in $q-d$ frame can be obtained as

$$\begin{bmatrix} v_{qC} \\ v_{dC} \end{bmatrix} = K_{TA}H_T(s) \begin{bmatrix} 1 & \frac{-\omega_b\bar{\omega}_e}{s} \\ \frac{\omega_b\bar{\omega}_e}{s} & 1 \end{bmatrix} \begin{bmatrix} i_{qL} \\ i_{dL} \end{bmatrix} \tag{11}$$

where

$$H_T(s) = \frac{s}{s^2 + (\omega_b\bar{\omega}_e)^2}. \tag{12}$$

Fig. 18 shows the block diagram used for the derivation of voltage across the series capacitor V_C from the line current I_L. The notch filter in this figure is used to eliminate the undamped natural frequency in the $H_T(s)$ transfer function located at $\omega_{tn} = \omega_b\bar{\omega}_e$. Moreover, in Fig. 18, $K_{TA} = \omega_b X_C$. In case the exact value of the X_C is not known, this gain can be used to tune the SSRDC in order to obtain the required SSR damping ratio.

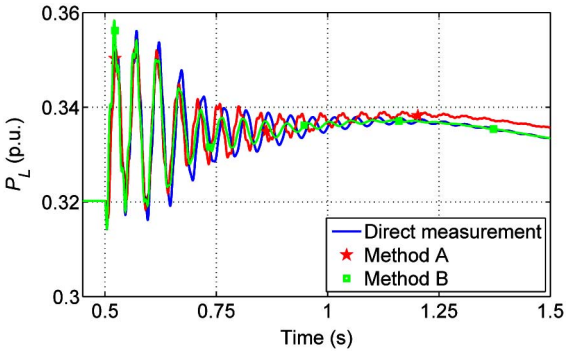

Fig. 20. Transmission line real power P_L obtained with direct measurement of V_C, method A, and method B.

B. Derivation From Instantaneous Line Current (Method B)

The relationship between the instantaneous line current and capacitor voltage is given as follows:

$$C\frac{dv_{C-abc}}{dt} = i_{L-abc}. \tag{13}$$

Equation (13) shows that the capacitor voltage can be estimated through the local current. Fig. 19 shows the block diagram used to estimate the voltage across the capacitor. The value of K_{TB} in Fig. 19 is equal to $\frac{1}{C}$. Even in case the exact value of the series capacitor is not known, the SSRDC can be tuned using K_T to obtain the required SSR damping ratio.

C. Simulation Results

In order to examine the effectiveness of methods A and B in estimating voltage across the series capacitor, Fig. 20 compares the transmission line power with the V_C as ICS for the SSRDC. In this figure, V_C is obtained using direct measurement, method A, and method B. As seen in this figure, both methods A and B can successfully estimate the voltage across the series capacitor.

VIII. Conclusion

In this paper, SSR mitigation in DFIG-based wind farm using RSC and GSC controllers is studied. First, using eigenvalue analysis, performed in MATLAB/Simulink and time-domain simulation, performed in PSCAD/EMTDC, it is shown that the series-compensated DFIG wind farm is highly unstable due to the SSR mode. Then, to mitigate the SSR, an SSRDC is designed using residue-based analysis and root-locus method, and the designed SSRDC is implemented at different points of the RSC and GSC controllers (see Figs. 4 and 5) in order to identify the optimum points within these controllers for the SSRDC implementation. The residue-based analysis is used to identify an optimum ICS to the SSRDC among three tested signals namely generator rotor speed ω_r, line real power P_L, and voltage across the series capacitor V_C, and root-locus method is used to compute the required SSRDC gain to stabilize the SSR mode, while verifying the residue-based analysis. Moreover, two methods are presented in order to estimate the voltage across the series capacitor, without measuring it directly.

The optimum ICS and optimum point in RSC and GSC controllers should enable the SSRDC to stabilize the SSR mode, without destabilizing or decreasing the stability of other system modes. In summary, the following results can be drawn regarding the optimum converter and ICS.

1) Using the SSRDC design method presented in this paper, ω_r and P_L can cause the SupSR mode or the electromechanical mode (or even both of them together) to go unstable, when used to stabilize the SSR mode, regardless of the insertion point chosen for the SSRDC implementation. It may be possible to successfully use these signals for SSR stabilization, but a more complex compensation would be required, losing the simplicity of the proposed proportional controller. The investigation of more complex compensation options is left as future work.
2) Neither of RSC controllers can be used to implement the SSRDC, regardless of what the ICS is.
3) All points of the GSC controllers can be used to implement the SSRDC, when the ICS is V_C.
4) With V_C as ICS, the implementation of SSRDC at points D_{GSC} through F_{GSC} requires a smaller SSR feedback gain compared to A_{GSC} through C_{GSC}.
5) Time-domain simulation in PSCAD/EMTDC verifies the SSRDC design process.

References

[1] J. Mohammadi, S. Vaez-Zadeh, S. Afsharnia, and E. Daryabeigi, "A combined vector and direct power control for DFIG-based wind turbines," *IEEE Trans. Sustain. Energy*, vol. 5, no. 3, pp. 767–775, Jul. 2014.

[2] H. A. Mohammadpour and E. Santi, "Modeling and control of gate-controlled series capacitor interfaced with a DFIG-based wind farm," *IEEE Trans. Ind. Electron.*, vol. 62, no. 2, pp. 1022–1033, Feb. 2015.

[3] M. Singh *et al.*, "Inter-area oscillation damping controls for wind power plants," *IEEE Trans. Sustain. Energy*, doi: 10.1109/ TSTE.2014.2348491, to be published.

[4] T. Ackermann, *Wind Power in Power Systems*. Hoboken, NJ, USA: Wiley, 2005.

[5] F. Besnard, K. Fischer, and L. B. Tjernberg, "A model for the optimization of the maintenance support organization for offshore wind farms," *IEEE Trans. Sustain. Energy*, vol. 4, no. 2, pp. 443–450, Apr. 2013.

[6] A. Hooshyar, M. Abdelkhalek, and E. F. El-Saadany, "Three-phase fault direction identification for distribution systems with DFIG-based wind DG," *IEEE Trans. Sustain. Energy*, vol. 5, no. 3, pp. 747–756, Jul. 2014.

[7] I. A. Gowaid, S. Abdel-Khalik, A. M. Massoud, and S. Ahmed, "Ride-through capability of grid-connected brushless cascade DFIG wind turbines in faulty grid conditions: A comparative study," *IEEE Trans. Sustain. Energy*, vol. 4, no. 4, pp. 1002–1015, Oct. 2013.

[8] M. A. Asha Rani, C. Nagamani, G. Saravana Ilango, and A. Karthikeyan, "An effective reference generation scheme for DFIG with unbalanced grid voltage," *IEEE Trans. Sustain. Energy*, vol. 5, no. 3, pp. 1010–1018, Jul. 2014.

[9] R. Andreoli de Marchi, P. S. Dainez, F. J. Von Zuben, and E. Bim, "A multilayer perceptron controller applied to the direct power control of a doubly fed induction generator," *IEEE Trans. Sustain. Energy*, vol. 5, no. 2, pp. 498–506, Apr. 2014.

[10] E. Ergun, D. V. Hertem, and R. Belmans, "Transmission system topology optimization for large-scale offshore wind integration," *IEEE Trans. Sustain. Energy*, vol. 3, no. 4, pp. 908–917, Oct. 2012.

[11] B. Silva, C. L. Moreira, L. Seca, Y. Phulpin, and J. A. Peas Lopes, "Provision of inertial and primary frequency control services using offshore multiterminal HVDC networks," *IEEE Trans. Sustain. Energy*, vol. 3, no. 4, pp. 800–808, Oct. 2012.

[12] R. E. Torres-Olguin, M. Molinas, and T. Undeland, "Offshore wind farm grid integration by VSC technology with LCC-Based HVDC Transmission," *IEEE Trans. Sustain. Energy*, vol. 3, no. 4, pp. 899–907, Oct. 2012.

[13] S. M. Muyeen, R. Takahashi, and J. Tamura, "Operation and control of HVDC-connected offshore wind farm," *IEEE Trans. Sustain. Energy*, vol. 1, no. 1, pp. 30–37, Apr. 2010.

[14] A. Moawwad, M. S. El Moursi, and W. Xiao, "A novel transient control strategy for VSC-HVDC connecting offshore wind power plant," *IEEE Trans. Sustain. Energy*, vol. 5, no. 4, pp. 1056–1069, Oct. 2014.

[15] M. A. Penalba, O. Gomis-Bellmunt, and M. Martins, "Coordinated control for an offshore wind power plant to provide fault ride through capability," *IEEE Trans. Sustain. Energy*, vol. 4, no. 4, pp. 1253–1261, Oct. 2014.

[16] N. G. Hingorani and L. Gyugi, Understanding FACTS. Piscataway, NJ, USA: IEEE Press, Apr., 2000.

[17] A. Moharana, R. K. Varma, and R. Seethapathy, "SSR alleviation by STATCOM in induction-generator-based wind farm connected to series compensated line," *IEEE Trans. Sustain. Energy*, vol. 5, no. 3, pp. 947–957, Jul. 2014. doi: 10.1109/TSTE.2014.2311072.

[18] H. A. Mohammadpour, S. M. H. Mirhoseini, and A. Shoulaie, "Comparative study of proportional and TS fuzzy controlled GCSC for SSR mitigation," in *Proc. Int. Conf. IEEE Power Eng. Energy Electr. Drives*, Mar. 18–20, 2009, pp. 564–569.

[19] H. A. Mohammadpour, M. R. Pahlavani, and A. Shoulaie, "On control of gate controlled series capacitor for SSR and power oscillation damping," in *Proc. IEEE Compat. Power Electron.*, May 20–22, 2009, pp. 196–203.

[20] M. Pahlavani and H. A. Mohammadpour, "Damping of sub-synchronous resonance and low-frequency power oscillation in a series-compensated transmission line using gate-controlled series capacitor," *Electr. Power Syst. Res.*, vol. 81, no. 2, pp. 308–317, Feb. 2011.

[21] K. R. Padiar, Analysis of Sub-synchronous Resonance in Power Systems. Norwell, MA, USA: Kluwer Academic, 1999.

[22] IEEE SSR Task Force, "First benchmark model for computer simulation of subsynchronous resonance," *IEEE Trans. Power App. Syst.*, vol. 96, no. 5, pp. 1562–1572, Sep./Oct. 1997.

[23] H. A. Mohammadpour and E. Santi, "Sub-synchronous resonance analysis in DFIG-based wind farms: Definitions and problem identification—Part I," in *Proc. IEEE Energy Convers. Congr. Expo.,* Sep. 2014, pp. 812–819.

[24] H. A. Mohammadpour and E. Santi, "Sub-synchronous resonance analysis in DFIG-based wind farms: Mitigation methods—TCSC, GCSC, and DFIG controllers—Part II," in *Proc. IEEE Energy Convers. Congr. Expo.*, Sep. 2014, pp. 1550–1557.

[25] L. Fan and Z. Miao, "Mitigating SSR using DFIG-based wind generation," *IEEE Trans. Sustain. Energy*, vol. 3, no. 3, pp. 349–358, Jul. 2012.

[26] C. Zhu, M. Hu, and Z. Wu, "Parameters impact on the performance of a double-fed induction generator-based wind turbine for sub-synchronous resonance control," *IET Renew. Power Gener.*, vol. 6, no. 2, pp. 92–98, Mar. 2012.

[27] Z. Miao, "Impedance-model-based SSR analysis for type 3 wind generator and series-compensated network," *IEEE Trans. Energy Convers.*, vol. 27, no. 4, pp. 984–991, Dec. 2012.

[28] L. Wang and L.-Y. Chen, "Reduction of power fluctuations of a large-scale grid-connected offshore wind farm using a variable frequency transformer," *IEEE Trans. Sustain. Energy*, vol. 2, no. 3, pp. 226–234, Jul. 2011.

[29] H. A. Mohammadpour, Y. J. Shin, and E. Santi, "SSR analysis of a DFIG-based wind farm interfaced with a gate-controlled series capacitor," in *Proc. 29th Annu. IEEE Appl. Power Electron. Conf. Expo.*, Mar. 2014, pp. 3110–3117.

[30] H. A. Mohammadpour, A. Ghaderi, and E. Santi, "Analysis of sub-synchronous resonance in doubly-fed induction generator-based wind farms interfaced with gate-controlled series capacitor," *IET Gener. Transmiss. Distrib.*, vol. 8, no. 12, pp. 1998–2011, Dec. 2014.

[31] P. Kundur, Power System Stability and Control. New York, NY, USA: McGraw-Hill, Inc., 1994.

[32] K. Chen, S. Tian, Y. Cheng, and L. Bai, "An improved MPPT controller for photovoltaic system under partial shading condition," *IEEE Trans. Sustain. Energy*, vol. 5, no. 3, pp. 978–985, Jul. 2014.

Hossein Ali Mohammadpour (S'10) received the B.Sc. and M.Sc. degrees both in electrical engineering power systems from Iran University of Science and Technology (IUST), Tehran, Iran, in 2006 and 2009, respectively, and received the Ph.D. degree in electrical engineering and electric power systems from the University of South Carolina, Columbia, SC, USA, in 2014.

He is currently a Postdoctoral Fellow with the University of South Carolina. His research interests include power systems stability and control, control of power electronics systems, renewable energy, smart grid, Flexible AC Transmission System (FACTS) technologies, and electric ship system modeling and analysis.

Enrico Santi (S'90–M'94–SM'02) received the Dr.Ing. degree in electrical engineering from the University of Padua, Padua, Italy, in 1988, and the M.S. and Ph.D. degrees from Caltech in 1989 and 1994, respectively.

He worked as a Senior Design Engineer with TESLAco from 1993 to 1998, where he was responsible for the development of various switching power supplies for commercial applications. Since 1998, he has been with the University of South Carolina, Columbia, SC, USA, where he is currently an Associate Professor with the Electrical Engineering Department. He has authored over 100 papers in power electronics and modeling and simulation in international journals and conference proceedings and holds two patents. His research interests include switched-mode power converters, advanced modeling and simulation of power systems, modeling and simulation of semiconductor power devices, and control of power electronics systems.